Storage and Reemission of Heralded Telecommunication-Wavelength Photons Using a Crystal Waveguide

Mohsen Falamarzi Askarani,[1,2,*] Marcel.li Grimau Puigibert,[1,3] Thomas Lutz,[1,4] Varun B. Verma,[5] Matthew D. Shaw,[6] Sae Woo Nam,[5] Neil Sinclair,[1,7] Daniel Oblak,[1] and Wolfgang Tittel[1,2]

[1] *Department of Physics & Astronomy and Institute for Quantum Science and Technology, University of Calgary, 2500 University Drive NW, Calgary, Alberta T2N 1N4, Canada*

[2] *QuTech, Delft University of Technology, Delft 2600, Netherlands*

[3] *University of Basel, Klingelbergstrasse 82, Basel CH-4056, Switzerland*

[4] *ETH Zürich, Otto-Stern-Weg 1, Zürich 8093, Switzerland*

[5] *National Institute of Standards and Technology, 325 Broadway, Boulder, Colorado 80305, USA*

[6] *Jet Propulsion Laboratory, California Institute of Technology, 4800 Oak Grove Drive, Pasadena, California 91109, USA*

[7] *California Institute of Technology, 1200 East California Boulevard, Pasadena, California 91125, USA*

(Received 8 May 2018; revised manuscript received 15 April 2019; published 21 May 2019)

Large-scale fiber-based quantum networks will likely employ telecommunication-wavelength photons of around 1550 nm wavelength to exchange quantum information between remote nodes, and quantum memories, ideally operating at the same wavelength, that allow the transmission distances to be increased, as key elements of a quantum repeater. However, the development of a suitable memory remains an ongoing challenge. Here, we demonstrate the storage and reemission of single heralded 1532-nm-wavelength photons using a crystal waveguide. The photons are emitted from a photon-pair source based on spontaneous parametric down-conversion and the memory is based on an atomic frequency comb of 6 GHz bandwidth, prepared through persistent spectral-hole burning of the inhomogeneously broadened absorption line of a cryogenically cooled erbium-doped lithium niobate waveguide. Despite currently limited storage time and efficiency, this demonstration represents an important step toward quantum networks that operate in the telecommunication band and the development of integrated (on-chip) quantum technology using industry-standard crystals.

DOI: 10.1103/PhysRevApplied.11.054056

I. INTRODUCTION

Many efforts toward future quantum networks [1] have focused on employing telecommunication-wavelength photons in the C band (1530–1565 nm) due to their suitability for connecting remote nodes via existing and low-loss fiber infrastructure. The synchronization of information in such nodes is enabled by quantum memories that allow the storage and later retrieval of quantum information [2]. As such, quantum memories are essential for the operation of quantum repeaters, which promise the transmission of quantum information over large distances [3].

The push to realize long-distance quantum communication has been enabled by significant progress in the development of quantum-optical technology [4]. However, a lot of this work is not compatible with C-band photons without the use of complexity-adding and potentially lossy frequency conversion [5]. To avoid this conversion step, supplementary efforts have focused on developing quantum technology that operates in the telecom C band, which has resulted in, for example, the development of efficient single-photon detectors [6] and single-photon sources [7]. Furthermore, significant progress toward quantum memories using various platforms has been made in the past decade [8]. One promising approach is based on cryogenically cooled rare-earth-ion-doped crystals, as they often feature suitable properties, such as long optical- and spin-coherence times [9]. Achievements include storage of entangled photons [10,11], teleportation into a quantum memory [12], storage in nanofabricated structures [13], and storage assisted by impedance-matched cavities [14,15]. In addition, quantum storage and signal processing has been demonstrated using thulium doped into an industry-standard titanium-indiffused lithium niobate waveguide [10]—a promising approach to efficient on-chip information processing. However, the development

*m.falamarziaskarani@tudelft.nl

of a C-band quantum memory, especially one that can be integrated on chip, has turned out to be a challenging task.

One class of materials that has the potential to fill this gap is that of erbium-doped crystals. They are unique in that they offer a ground-to-excited-level transition at around 1532 nm wavelength and optical coherence times up to 4.4 ms—the longest in any optical transition in a solid [16]. This has prompted the demonstration of a photon-echo quantum-memory protocol with attenuated laser pulses at the single-photon level in $Er:Y_2SiO_5$ [17] but not for nonclassical (single-photon) light. The difficulty with erbium-doped materials is the relatively long lifetime of the excited level—up to approximately 11 ms—compared to that of sublevels within the ground-state manifold (around 100 ms). This makes optical pumping to the latter—a necessary step in photon-echo quantum memory [2]—challenging and poses a significant obstacle to achieving high storage efficiency. This problem is partially solved in Er-doped fibers, which, due to their amorphous (rather than crystalline) structure, feature reduced spin-spin interactions and, as a result, extended ground-state (Zeeman-level) lifetimes [18]. This has allowed recent demonstrations of the storage and reemission of nonclassical and entangled states of light at telecommunication wavelengths [19]. However, despite the appeal of Er-doped fibers for all-fiber implementations, the decoherence arising from their amorphous structure [20] currently restricts the storage time to about 50 ns, although improvements may be possible at ultralow temperatures.

Other promising approaches to overcoming the limitations of erbium are the use of magnetic fields of several tesla, where ground-state lifetimes can exceed 1 min [21], and crystals inside cavities with high quality factors and small mode volumes, which reduce the excited-state lifetime by means of the Purcell effect [22]. But despite a lot of research aimed at developing quantum memory at telecommunication wavelengths, the storage and reemission of nonclassical light using an erbium-doped crystal—in particular, a crystalline waveguide that can be integrated with telecommunication-industry devices—remains a goal that is yet to be achieved.

Here, we demonstrate quantum memory for heralded single photons at 1532.05 nm wavelength using an Er-doped lithium niobate waveguide created through titanium indiffusion. The heralded photons are generated using a photon-pair source based on spontaneous parametric down-conversion (SPDC) and storage and reemission relies on the atomic frequency comb (AFC) protocol [23] and optical pumping into superhyperfine levels, which have previously not been exploited toward this end. The nonclassical nature of the reemitted (heralded) photons is verified by measuring the cross-correlation function $g_{12}^{(2)}$ with the heralding photons.

II. THE AFC QUANTUM-MEMORY PROTOCOL

The storage and reemission process of single photons is based on the AFC protocol, which has underpinned a lot of progress toward efficient and broadband quantum memory during the past decade. For example, storage times as long as milliseconds [24], efficiencies as high as 56% [14], storage bandwidths of several gigahertz [10], and fidelities up to 99.9% [25] have been achieved.

An atomic frequency comb is comprised of a series of narrow spectral absorption lines that are equidistantly detuned by Δ (a "comb" of absorption features) [23]. It can be prepared from an inhomogeneously broadened absorption line of rare-earth ions by frequency-selective optical pumping of population into long-lived auxiliary levels. The absorption of a photon by an AFC leads to a collective atomic excitation described as follows:

$$|\Psi\rangle_A = \frac{1}{\sqrt{N}} \sum_{j=1}^{N} c_j e^{-i2\pi\delta_j t} e^{ikz_j} |g_1, \ldots e_j, \ldots g_N\rangle. \quad (1)$$

Here, N is the number of ions and δ_j the detuning of the jth ion's transition frequency with respect to the carrier frequency of the incoming photon. The longitudinal position of the ions is denoted by z_j and the coefficient c_j is related to the ion's excitation probability (i.e., its position and transition frequency). After absorption, each term in Eq. (1) accumulates a phase that depends on the detuning $\delta_j = m_j \Delta$, where m_j is an integer. Consequently, all terms coherently rephase at a time $\tau = 1/\Delta$, leading to collective reemission of the photon in its original quantum state. Under certain conditions, the reemission process can reach unit efficiency [23,26,27].

III. SPECTROSCOPIC CHARACTERIZATION

For AFC-based quantum-state storage in an ensemble of absorbers—in our case, rare-earth ions doped into a crystal—the storage medium has to meet several criteria. In addition to a suitable level structure (e.g., absorption at the desired wavelength), they include an inhomogeneously broadened absorption profile with a bandwidth that exceeds the inverse duration of the photons to be stored; the possibility of optical pumping into long-lived auxiliary shelving levels (so-called persistent spectral-hole burning); and a coherence time in excess of the desired storage time.

To date, only a few spectroscopic studies of the low-temperature properties of the 1532-nm $^4I_{15/2} \leftrightarrow {}^4I_{13/2}$ transition of erbium-doped lithium niobate—both in bulk crystals as well as in waveguides created by means of titanium indiffusion (for details about the waveguide fabrication, see Appendix A)—have been reported [9,28–31]. For light polarized orthogonal to the crystal's c axis ($\mathbf{E}\perp\mathbf{c}$), the 1532-nm transition of $Er:LiNbO_3$ features a 180-GHz-wide inhomogeneously broadened line, a 2-ms population

lifetime of the $^4I_{13/2}$ level, and, at a temperature of 1.6 K and a magnetic field of 50 kG oriented parallel to the c axis (**B**‖**c**), an optical coherence time of 117 μs [9,30]. The same transition of Er^{3+} has been studied in a Ti^{4+}:$LiNbO_3$ waveguide at 3 K, resulting in a 250-GHz-wide inhomogeneously broadened line, a population lifetime matching that of the bulk material, and a coherence lifetime of 18.2 μs in a 4 kG field oriented **B**‖**c** [28]. We expect that the coherence lifetime of the waveguide increases and eventually equals that of the bulk crystal at lower temperatures and under the application of an optimized magnetic field, similarly to what we previously observed for a Tm^{3+}:Ti^{4+}:$LiNbO_3$ waveguide compared to bulk Tm^{3+}:$LiNbO_3$ [32].

To identify long-lived auxiliary levels with lifetimes that significantly exceed that of the $^4I_{13/2}$ excited level, we perform spectral-hole burning (SHB) to study the level structure and dynamics of Er^{3+}:Ti^{4+}:$LiNbO_3$ at various magnetic fields. Toward this end, we excite the inhomogeneously broadened 1532-nm transition using a narrow-band laser and then read the frequency-dependent absorption profile by scanning the laser over a spectral interval centered at the excitation frequency. An absorption spectrum obtained at a magnetic field of 19 kG and taken after 30 s—a time that exceeds by far the lifetime of the $^4I_{13/2}$ level—is shown in Fig. 1(a). Regions of increased (decreased) transparency that are detuned from the central hole (at the excitation frequency) are referred to as side (anti)holes—additional studies with varying waiting times between excitation and read-out reveal that they persist for several minutes.

To determine the cause of the level splitting and hence the substructure, we perform SHB at different magnetic fields with **B**‖**c**. Figure 1(b) depicts the field-dependent detunings for three pairs of distinguishable side holes. Fits yield values of 1.15 ± 0.01, 1.721 ± 0.006, and 0.572 ± 0.002 kHz/G, respectively. This agrees with the superhyperfine coupling between the Er^{3+} electronic spin ($S = 1/2$) and the nuclear spins of ^{93}Nb ($I = 9/2$), ^{7}Li ($I = 3/2$), and ^{6}Li ($I = 1$) in the host crystal that was previously reported for an Er^{3+}:$LiNbO_3$ bulk crystal [30]. The side-hole positions are determined by the excited-level splitting, whereas the position of the antiholes are given by the ground-state splitting as well as by differences between ground- and excited-state splittings. These observations suggest the possibility for persistent spectral-hole burning using superhyperfine levels.

In addition, we also find evidence of population transfer into long-lived electronic Zeeman levels of erbium at small magnetic fields. However, a large absorption background in AFCs exceeding 1 GHz bandwidth prevents us from using these levels for shelving. For more information, see [33].

IV. HERALDED SINGLE-PHOTON STORAGE

To demonstrate the storage of single photons in the Er-doped crystal, we apply a magnetic field of 16.5 kG and **B**‖**c** across the crystal and create an AFC with approximately 21 MHz tooth spacing, i.e., a storage time of $\tau = 48$ ns. The tooth spacing is chosen such that the comb periodicity coincides with the excited-level splitting caused by the superhyperfine interactions between the erbium electronic spin and the nuclear spin of ^{7}Li and ^{93}Nb. The finesse of the comb—the ratio of the tooth width γ to the tooth spacing Δ—is two. Combined with the optical depths of the comb and the background obtained from the AFC trace in Fig. 2, it limits the AFC storage efficiency

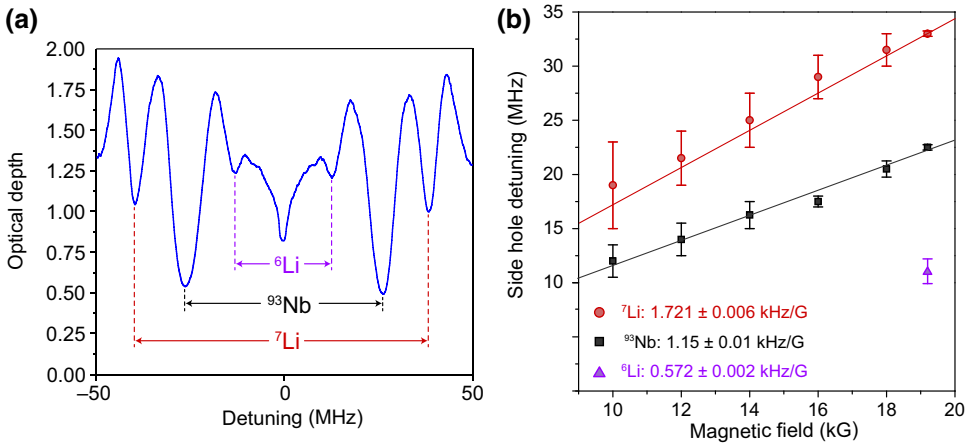

FIG. 1. (a) The optical depth over a 100-MHz-wide spectral range centered at 1532.05 nm after applying a 19 kG magnetic field. Side holes due to the interaction between the Er^{3+} electronic spin and ^{93}Nb, ^{6}Li and ^{7}Li nuclear spins are visible. The apparent side holes at ±50 MHz are due to an imperfect frequency sweep. (b) Detuning of ^{7}Li and ^{93}Nb side holes as a function of the magnetic field. The side holes for ^{6}Li are resolved only at the highest field. The uncertainty bars indicate the difference between the detunings of the positive and negative side holes compared to the central hole.

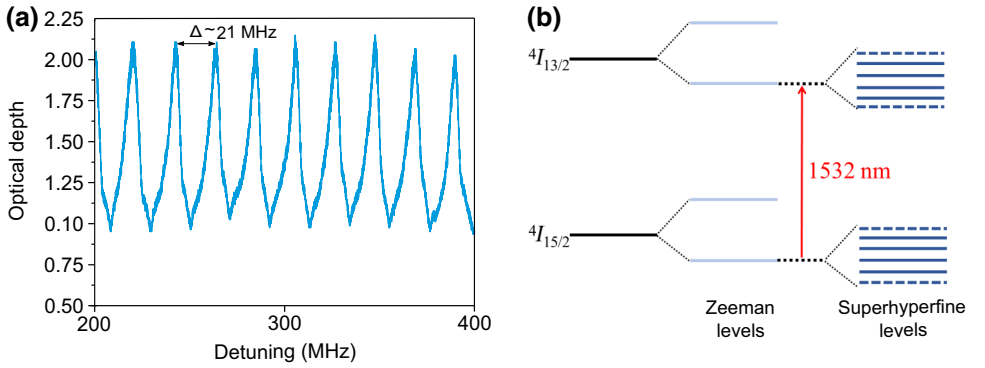

FIG. 2. (a) A 200-MHz-wide section of our 6-GHz-bandwidth AFC. (b) A simplified energy-level diagram of erbium in lithium niobate. An AFC can be created by redistributing—optically pumping through the $^4I_{13/2}$ excited level—ions between superhyperfine levels of the $^4I_{15/2}$ ground-state manifold.

to around 1%. However, insufficient laser intensity at large detunings and hence nonoptimized hole burning leads to a nonuniform AFC and an averaged AFC efficiency of around 0.1%.

Next, we generate 6 GHz wide heralded single photons at 1532 nm wavelength using SPDC of short 523-nm laser pulses in a periodically poled lithium niobate crystal. This nonlinear process results in the probabilistic generation of photon pairs at 795 and 1532 nm wavelength and hence detecting a 795-nm photon indicates (heralds) the presence of another photon at 1532 nm. (The experimental setup is outlined in Fig. 3 and its components are described in detail in Appendix C.) These photons are then sent into, absorbed (stored) in, and reemitted from the erbium memory after the preprogrammed time delay of 48 ns (see Fig. 4).

To demonstrate the nonclassical nature of the reemitted photons and hence the memory, we measure the second-order cross-correlation function $g_{12}^{(2)} = P_{12}/P_1P_2$. Here, the probability of detecting a coincidence between the two photons is P_{12} and P_1 (P_2) are the probabilities of detecting the two photons individually (for more details, see Ref. [34]). To verify the presence of nonclassical correlations,

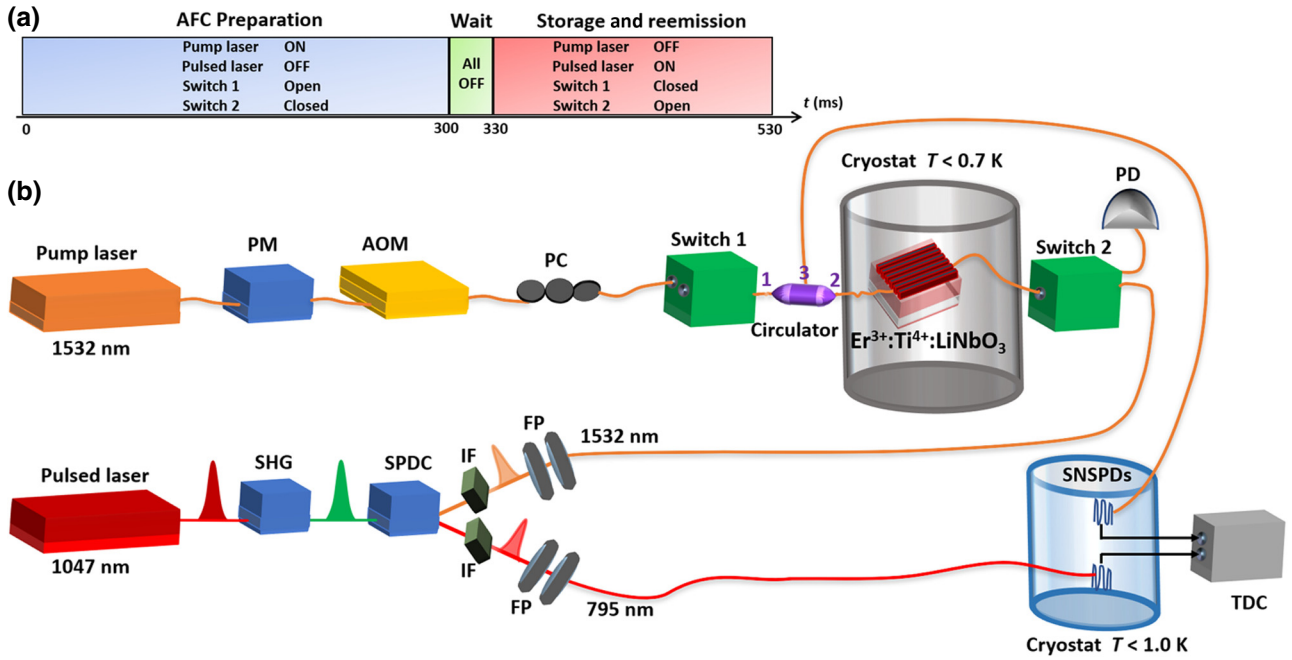

FIG. 3. (a) The experimental timing sequence. The sequence is continuously repeated during the experimental run. Switch 2 is closed [and connected to the photodetector (PD)] during the AFC preparation for monitoring the AFC structure and for recording the frequency-dependent optical depth shown in Figs. 1(a) and 2(b). The experimental setup consists of two main parts. The part depicted in the top half allows for optical pumping (spectral-hole burning) and AFC generation—it consists of a pump laser, a phase modulator (PM), an acousto-optic modulator (AOM), a polarization controller (PC), optical switches, a circulator, and a PD. The part in the bottom half depicts the heralded single-photon generation and the detection setup—it consists of a pulsed pump laser, second-harmonic generation (SHG), spontaneous parametric down-conversion (SPDC), long-pass filters (LF), Fabry-Perot cavities (FP), superconducting nanowire single-photon detectors (SNSPD), and a time-to-digital converter (TDC). For details of all components, see Appendices C–E.

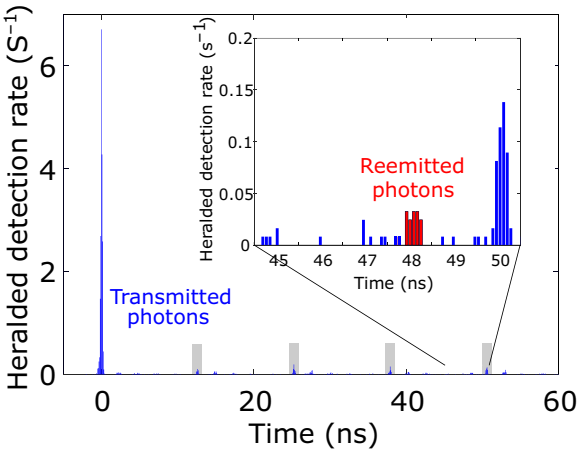

FIG. 4. The storage and reemission of heralded single photons at telecommunication wavelength. The histogram depicts the time-resolved rate of coincidence detections of heralding 795-nm and heralded 1532-nm photons. The overall acquisition time is 2 min. The time axis is defined relative to the detection of 1532-nm photons that are directly transmitted (not absorbed) by the memory. Stored photons are reemitted after 48 ns and cause the coincidence peak highlighted in red in the enlargement. The number of coincidences in the 500-ps-long window is 18 ± 4.24, clearly exceeding the background of 1.9 ± 0.45 per 500 ps window, obtained by averaging coincidences between 44.5 ns and 49.5 ns. The coincidence peaks at $t \approx 2.5$, 5, 7.5, and 10 ns are due to spurious temporal modes of the pump laser—a consequence of imperfect alignment of the laser cavity—causing additional photon-pair generation by the SPDC crystal. The sequence of coincidence-detection peaks is repeated every 12.5 ns, matching the 80 MHz repetition rate of the pulsed SPDC pump laser. These repeated patterns, often referred to as accidental coincidences, are due to the detection of photons belonging to pairs that have been generated during different laser cycles.

$g_{12}^{(2)}$ must be greater than 2 [34,35]. First, bypassing the waveguide, we determine $g_{12}^{(2)}$ of our photon-pair source (without additional storage) to be around 20. It is limited by multipair emissions that are caused by the high pump intensity [35]. Repeating the measurement with reemitted photons, we then find that $g_{12}^{(2)} = 7.1 \pm 4$ (for details, see Appendix E). This demonstrates that nonclassical correlations between the members of photon pairs remain throughout the storage process, i.e., that the memory indeed operates in the quantum domain.

V. DISCUSSION

While this result is promising, several improvements are necessary to create a quantum memory that can be used in a quantum repeater. First, the total system efficiency—evaluated by comparing the heralded photon-detection rates measured with the full setup with that after circumventing the cryostat (including the memory)—is currently only of around 0.01%. This number is limited by a coupling efficiency of around 10% and, as mentioned above, the efficiency of the storage and reemission process (i.e., that of the AFC itself) of 0.1%. The latter is determined by several factors, including the lack of phase matching that allows the triggering of backward emission [23], low finesse ($F = 2$) of the AFC due to the chosen pumping scheme, insufficient optical depth of the comb teeth, and a remaining absorption background, especially at large detuning.

The coupling efficiency can be improved by optimized matching of the modes guided by the fiber and the waveguide. Furthermore, the limited optical depth and the lack of phase matching can be countered with an impedance-matched cavity [26,27]. However, this solution is not beneficial without reducing the remaining background loss, which we attribute to the complexity of the superhyperfine-level structure and the possibility of laser-induced enhancement of spin relaxation [31,33]—an effect that we have previously observed and mitigated in the creation of AFCs in Tm^{3+}:Ti^{4+}:$LiNbO_3$ [32].

We believe that further characterization of the atomic-level structure and population dynamics, in particular through more detailed SHB measurements (e.g., with varying magnetic field strength and orientation), as well as optimization of the AFC preparation steps (e.g., using back pumping [36] or spin-mixing methods [37]), will allow a significant reduction of the background absorption. Another possibility may be exploration of persistent spectral-hole burning into Zeeman levels [33]. Furthermore, wavelength-dependent measurements may allow the identification of ions belonging to different magnetic subclasses and featuring favorable (superhyperfine or Zeeman) levels. Ultimately, a lower sample temperature and erbium-doping concentration could allow for more efficient SHB in addition to suppressing decoherence caused, e.g., by spin flip-flops.

Another limitation of the current demonstration is the storage time, which, as described above, is indirectly determined by the strength of the external magnetic field. More precisely, the field sets the splittimg of the superhyperfine levels, which in turn determines the frequency spacing between peaks and troughs of the AFC and hence the comb periodicity Δ. If this were the only factor, then the use of small magnetic fields would allow for arbitrarily small tooth spacing and hence arbitrarily long storage times. However, the minimum tooth spacing (and hence the maximum storage time) is given by the material's homogeneous line width (the inverse of the coherence time, possibly rendered worse by spectral diffusion) and—being the limiting factor in our case—instability of the frequency of the (free-running) laser used for spectral-hole burning. We estimate that locking to a stable reference cavity would allow the storage time to be increased to a few microseconds, which could be further increased to hundreds of microseconds by further reducing the temperature.

Finally, we note that our current approach does not allow photons to be reemitted on demand, which requires an additional step, i.e., the reversible coherent mapping to a third long-lived level [38]. Nonetheless, applications such as quantum repeaters may utilize memories of fixed storage times provided that spectral or spatial multiplexing is performed [39].

VI. CONCLUSION

In conclusion, we demonstrate the storage and reemission of heralded single photons at telecommunication wavelength using a cryogenically cooled erbium-doped lithium niobate waveguide. The nonclassical nature of the storage process is demonstrated by a measurement of the cross-correlation coefficient between the heralding and the heralded photons after reemission. We employ an AFC that is based on optical pumping of atomic population into superhyperfine ground levels and we detail the limitations as well as possible improvements of our memory; in particular, its limited storage efficiency. Our work is a step toward on-chip quantum-network technology operating in the important telecommunication C band using standard telecommunication-industry materials.

APPENDIX A: ER-DOPED LITHIUM NIOBATE WAVEGUIDE

To fabricate the Er^{3+}:Ti^{4+}:$LiNbO_3$ waveguide, z-cut congruent $LiNbO_3$ is Er doped over a length of 10 mm by indiffusion of a vacuum-deposited (electron-beam evaporated) 8-nm-thick Er layer at 1130,$^\circ$ C for 150 h in an Ar atmosphere. This step is followed by a post-treatment in oxygen (1 h) to obtain a full reoxidization of the crystal. Er substitutes for Li when incorporated into the $LiNbO_3$ lattice. The indiffusion results in a 3.6×10^{19} cm^{-3} near-surface concentration and a Gaussian concentration profile that features a 1/e penetration depth of 8.2 μm [40]. Next, the waveguide is created by indiffusion of Ti. To do this, a 98-nm-thick titanium layer is deposited on the Er-doped surface of the $LiNbO_3$ substrate using electron-beam evaporation. From this layer, 7-μm-wide Ti strips are defined by photolithography and chemical etching and subsequently indiffused at 1060,$^\circ$ C for 8.55 h. This process leads to a single-mode waveguide with a 4.5×3 μm full-width-at-half-maximum intensity distribution for transverse magnetic polarization. Note that an analogous procedure, which is detailed in Ref. [10], is used to fabricate the similar Tm^{3+}:Ti^{4+}:$LiNbO_3$ waveguide.

For our experiments, the Er^{3+}:Ti^{4+}:$LiNbO_3$ waveguide is mounted in an adiabatic demagnetization refrigerator that can be operated at temperatures of around 0.6 K (Fig. 3). A magnetic field oriented $\mathbf{B}\|\mathbf{c}$ of up to 20 kG is applied using a solenoid. Light is coupled into and out of the waveguide by fiber butt coupling. The overall in-out coupling transmission of our cryogenic setup is around 10% (measured at a wavelength of 1532.05 nm).

APPENDIX B: SHB AND AFC PREPARATION

Time-dependent SHB is performed by exciting a subset of ions within a few-megahertz-broad spectral region of the inhomogeneously broadened absorption line using continuous-wave laser light at 1532.05 nm wavelength. The experimental setup is depicted in the top half of Fig. 3(b). Optical pumping then leads to a modification of the absorption profile, which is characterized by sweeping the frequency of the light across the spectral hole using a phase modulator and serrodyne modulation. This allows characterization of level spacings and, if repeated after various delays, population dynamics.

The AFC is generated by optical pumping during 300 ms, as illustrated by the timing sequence in Fig. 3(a). During this stage, the laser light is frequency swept over a 6 GHz bandwidth by serrodyne phase modulation while its intensity is modulated using an AOM. This procedure creates features of high (low pump-power intensity) and low (high pump-power intensity) absorption, as shown in Fig. 2 for a magnetic field of 16.5 kG and $\mathbf{B}\|\mathbf{c}$. A 30 ms time delay following the optical-pumping step [see Fig. 3(a)] ensures that no noise-inducing photons that are spontaneously emitted from the $^4I_{13/2}$ excited level mask the stored and reemitted photons. Finally, photons are repetitively stored and reemitted after 48 ns during a 200 ms time interval [see Fig. 3(a)]. The closing of the first optical switch (which is open during the AFC preparation) in conjunction with the circulator allows suppression of the stray pump light during the storage and reemission of the heralded single photons. Note that the light polarization and the magnetic field orientation are, respectively, set perpendicular and parallel to the c axis of the crystal, i.e., $\mathbf{E}\perp\mathbf{c}$ and $\mathbf{B}\|\mathbf{c}$.

APPENDIX C: SPDC-BASED HERALDED SINGLE-PHOTON SOURCE

As shown in Fig. 3, the creation of photon pairs begins with a mode-locked laser that emits pulses of 6 ps duration at a rate of 80 MHz and a wavelength of 1047 nm. These pulses are frequency doubled to 523.5 nm by means of second-harmonic generation using a periodically poled lithium niobate (PPLN) crystal and then used to pump a second PPLN crystal phase matched for SPDC and creating frequency-correlated photon pairs at 795 and 1532 nm wavelength. After passing through an interference filter that removes the remaining 523-nm light, a dichroic mirror separates the photons from each pair. Finally, the bandwidth of each photon is reduced by filtering: we employ a 12- (6-)GHz-bandwidth fiber-Bragg grating (Fabry-Perot

filter) for filtering the 1532- (795-)nm photons. The 1532-nm photons are coupled into the waveguide (the second optical switch is open at this stage) and then stored. After reemission, they are detected by a superconducting nanowire single-photon detector (SNSPD) [41]. The heralding 795-nm photon is directly detected by another SNSPD.

APPENDIX D: DATA ACQUISITION AND $g^{(2)}$ MEASUREMENT

To collect data, we employ a start-stop triggering method using a time-to-digital converter (TDC). The TDC starts with the detection of the heralding 795-nm photons and it stops with the detection of heralded 1532-nm photons after being transmitted through, or reemitted from, the waveguide. The TDC generates a histogram (shown in Fig. 4) that indicates the number of coincidence detections as a function of the time delay between the start and the stop.

The measured coincidence rate before adding the memory is around 2300 s^{-1}. It is determined by the repetition rate of the pump laser (80 MHz), the mean photon-pair generation probability per pump pulse (1.6%), and several factors that limit the probability of detecting the created photons. They are the coupling efficiencies into fiber of around 70% for photons of both wavelengths; transmission of the photons through long-pass filters (85% for both wavelengths) and Fabry-Perot cavities (40% and 60%), bandwidth mismatch between the pump and the down-converted photons (17% and 35%) [42]; and the detection efficiencies of the single-photon detectors, of around 70%. All brackets denote first the value for 795-nm and then for 1532-nm photons, respectively. The multiplication of these factors leads to a predicted coincidence rate of 3170 s^{-1}—not far from the measured result. We attribute the difference to loss in fiber connectors and underestimation of the effect of bandwidth mismatch. Inclusion of the quantum-memory-system efficiency of 0.01% and 33% extra loss due to an additional optical switch and a circulator then leads to a calculated coincidence rate for reemitted photons of around 0.21 s^{-1}. This approximately matches the experimental value of 0.16 s^{-1}, which can be extracted from the coincidence peak centered around 48 ns in Fig. 4.

As explained in more detail in Ref. [43], the cross-correlation function $g_{12}^{(2)}$ can be evaluated directly from the histogram by comparing the true and accidental coincidence rates:

$$g_{12}^{(2)} = \frac{P_{12}}{P_1 P_2} = \frac{R_{\text{true}}}{R_{\text{acc}}}.$$

Here, R_{true}, which is proportional to P_{12}, denotes the coincidence-detection rate of photons emitted simultaneously. These coincidences are represented by the peak at $t = 48$ ns. Furthermore, R_{acc} denotes the rate of accidental coincidences—it is proportional to $P_1 P_2$ and the coincidences are represented by the peaks highlighted in gray in Fig. 4. For increased accuracy, we evaluate R_{acc} by averaging over five accidental coincidence peaks.

We note that an adsorber that is part of the cryogenic system broke shortly after we started measuring. This made it impossible to improve the data depicted in Fig. 4 and hence the cross-correlation function.

APPENDIX E: SUPERCONDUCTING NANOWIRE SINGLE-PHOTON DETECTORS (SNSPDs)

The SNSPDs used in our experiment feature a detection efficiency of around 70%, a time resolution of around 100 ps, a dead time of approximately 100 ns, and a dark-count rate of 10–20 Hz. The signal created by each SNSPD is first amplified, shaped to a square pulse by a comparator, and then sent to a digital-delay generator. The generator's two outputs are connected to the TDC and a counter.

ACKNOWLEDGMENTS

We thank Wolfgang Sohler, Mathew George, and Raimund Ricken for providing the Er^{3+}:Ti^{4+}:$LiNbO_3$ waveguide, Francesco Marsili for assistance with development of the SNSPDs, Jakob H. Davidson for help with aligning the waveguide, and Gustavo Amaral and Erhan Saglamyurek for useful discussions. This work is funded through Alberta Innovates Technology Futures (AITF), the National Science and Engineering Research Council of Canada (NSERC), and the Defense Advanced Research Projects Agency (DARPA) Quiness program. W.T. furthermore acknowledges funding by the Netherlands Organization for Scientific Research (NWO) and as a Senior Fellow of the Canadian Institute for Advanced Research (CIFAR), and V.B.V. and S.W.N. partial funding for detector development from the Defense Advanced Research Projects Agency (DARPA) Information in a Photon (InPho) program. Part of the detector research was carried out at the Jet Propulsion Laboratory, California Institute of Technology, under a contract with the National Aeronautics and Space Administration (NASA).

[1] H. J. Kimble, The quantum internet, Nature **453**, 1023 (2008).
[2] A. I. Lvovsky, B. C. Sanders, and W. Tittel, Optical quantum memory, Nat. Phot. **3**, 706 (2009).
[3] N. Sangouard, C. Simon, H. De Riedmatten, and N. Gisin, Quantum repeaters based on atomic ensembles and linar optics, Rev. Mod. Phys. **83**, 33 (2011).
[4] J. L. O'Brien, A. Furusawa, and J. Vučković, Photonic quantum technologies, Nat. Phot. **3**, 687 (2009).
[5] S. Tanzilli, W. Tittel, M. Halder, O. Alibart, P. Baldi, N. Gisin, and H. Zbinden, A photonic quantum information interface, Nature **437**, 116 (2005).

[6] C. M. Natarajan, M. Tanner, and R. H. Hadfield, Superconducting nanowire single-photon detectors: Physics and applications, Supercond. Sci. Technol. **25**, 063001 (2012).

[7] T. Müller, J. Skiba-Szymanska, A. B. Krysa, J. M. Felle, M. Anderson, R. M. Stevenson, J. Heffernan, D. A. Ritchie, and A. J. Shields, A quantum light-emitting diode for the standard telecom window around 1550 nm, Nat. Comms. **9**, 862 (2018).

[8] F. Bussières, N. Sangouard, M. Afzelius, H. De Riedmatten, C. Simon, and W. Tittel, Prospective applications of optical quantum memories, J. Mod. Opt. **60**, 1519 (2013).

[9] C. W. Thiel, T. Böttger, and R. L. Cone, Rare-earth-doped materials for applications in quantum information storage and signal processing, J. Lumin. **131**, 353 (2011).

[10] E. Saglamyurek, N. Sinclair, J. Jin, J. A. Slater, D. Oblak, F. Bussieres, M. George, R. Ricken, W. Sohler, and W. Tittel, Broadband waveguide quantum memory for entangled photons, Nature **469**, 512 (2011).

[11] C. Clausen, I. Usmani, F. Bussières, N. Sangouard, M. Afzelius, H. De Riedmatten, and N. Gisin, Quantum storage of photonic entanglement in a crystal, Nature **469**, 508 (2011).

[12] F. Bussières, C. Clausen, A. Tiranov, B. Korzh, V. B. Verma, S. W. Nam, F. Marsili, A. Ferrier, P. Goldner, H. Herrmann, and C. Silberhorn, Quantum teleportation from a telecom-wavelength photon to a solid-state quantum memory, Nat. Phot. **8**, 775 (2014).

[13] T. Zhong, J. M. Kindem, J. G. Bartholomew, J. Rochman, I. Craiciu, E. Miyazono, M. Bettinelli, E. Cavalli, V. Verma, S. W. Nam, F. Marsili, M. D. Shaw, A. D. Beyer, and A. Faraon, Nanophotonic rare-earth quantum memory with optically controlled retrieval, Science **357**, 1392 (2017).

[14] M. Sabooni, S. TornibueKometa, A. Thuresson, S. Kröll, and L. Rippe, Cavity-enhanced storage—preparing for high-efficiency quantum memories, N. J. Phys. **15**, 035025 (2013).

[15] P. Jobez, I. Usmani, N. Timoney, C. Laplane, N. Gisin, and M. Afzelius, Cavity-enhanced storage in an optical spin-wave memory, N. J. Phys. **16**, 083005 (2014).

[16] T. Böttger, C. W. Thiel, R. L. Cone, and Y. Sun, Effects of magnetic field orientation on optical decoherence in Er3+:Y_2 SiO_5, Phys. Rev. B **79**, 115104 (2009).

[17] B. Lauritzen, J. Minář, H. De Riedmatten, M. Afzelius, N. Sangouard, C. Simon, and N. Gisin, Telecommunication-Wavelength Solid-State Memory at the Single Photon Level, Phys. Rev. Lett. **104**, 080502 (2010).

[18] E. Saglamyurek, T. Lutz, L. Veissier, M. P. Hedges, C. W. Thiel, R. L. Cone, and W. Tittel, Efficient and long-lived Zeeman-sublevel atomic population storage in an erbium-doped glass fiber, Phys. Rev. B **92**, 241111(R) (2015).

[19] E. Saglamyurek, J. Jin, V. B. Verma, M. D. Shaw, F. Marsili, S. W. Nam, D. Oblak, and W. Tittel, Quantum storage of entangled telecom-wavelength photons in an erbium-doped optical fibre, Nat. Phot. **9**, 83 (2015).

[20] L. Veissier, M. Falamarzi, T. Lutz, E. Saglamyurek, C. W. Thiel, R. L. Cone, and W. Tittel, Optical decoherence and spectral diffusion in an erbium-doped silica glass fiber featuring long-lived spin sublevels, Phys. Rev. B **94**, 195138 (2016).

[21] M. Rančić, M. P. Hedges, R. L. Ahlefeldt, and M. J. Sellars, Coherence time of over a second in a telecom-compatible quantum memory storage material, Nat. Phys. **14**, 50 (2018).

[22] E. Miyazono, T. Zhong, I. Craiciu, J. M. Kindem, and A. Faraon, Coupling of erbium dopants to yttrium orthosilicate photonic crystal cavities for on-chip optical quantum memories, Appl. Phys. Lett. **108**, 011111 (2016).

[23] M. Afzelius, C. Simon, H. De Riedmatten, and N. Gisin, Multimode quantum memory based on atomic frequency combs, Phys. Rev. A **79**, 052329 (2009).

[24] P. Jobez, C. Laplane, N. Timoney, N. Gisin, A. Ferrier, P. Goldner, and M. Afzelius, Coherent Spin Control at the Quantum Level in an Ensemble-Based Optical Memory, Phys. Rev. Lett. **114**, 230502 (2015).

[25] Z. Q. Zhou, W. B. Lin, M. Yang, C. F. Li, and G. C. Guo, Realization of Reliable Solid-State Quantum Memory for Photonic Polarization Qubit, Phys. Rev. Lett. **108**, 190505 (2012).

[26] M. Afzelius and C. Simon, Impedance-matched cavity quantum memory, Phys. Rev. A **82**, 022310 (2010).

[27] S. A. Moiseev, S. N. Andrianov, and F. Gubaidullin, Efficient multimode quantum memory based on photon echo in an optimal QED cavity, Phys. Rev. A **82**, 022311 (2010).

[28] A. Delfan Abazari, M.Sc. thesis, University of Calgary, 2009.

[29] C. W. Thiel, R. M. Macfarlane, R. L. Cone, Y. Sun, T. Böttger, K. D. Merkel, and W. R. Babbitt, in *10th Intl Meeting on Hole Burning, Single Molecule, and Related Spectroscopies: Science and Applications* (HBSM, 2009).

[30] C. W. Thiel, R. M. Macfarlane, T. Böttger, Y. Sun, R. L. Cone, and W. R. Babbitt, Optical decoherence and persistent spectral hole burning in Er3+:$LiNbO_3$, J. Lumin. **130**, 1603 (2010).

[31] C. W. Thiel, Y. Sun, R. M. Macfarlane, T. Böttger, and R. L. Cone, Rare-earth-doped $LiNbO_3$ and $KTiOPO_4$ (KTP) for waveguide quantum memories, J. Phys. B: Atomic Mol. Opt. Phys. **45**, 124013 (2012).

[32] N. Sinclair, D. Oblak, C. W. Thiel, R. L. Cone, and W. Tittel, Properties of a Rare-Earth-Ion-Doped Waveguide at Sub-Kelvin Temperatures for Quantum Signal Processing, Phys. Rev. Lett. **118**, 100504 (2017).

[33] M. F. Askarani, T. Lutz, M. G. Puigibert, N. Sinclair, D. Oblak, and W. Tittel, Persistent atomic frequency comb based on Zeeman sub-levels of an erbium-doped crystalline waveguide (to be published).

[34] S. Fasel, O. Alibart, S. Tanzilli, P. Baldi, A. Beveratos, N. Gisin, and H. Zbinden, High-quality asynchronous heralded single-photon source at telecom wavelength, New J. Phys. **6**, 163 (2004).

[35] P. R. Tapster and J. G. Rarity, Photon statistics of pulsed parametric light, J. Mod. Opt. **45**, 595 (1998).

[36] M. Nilsson, L. Rippe, S. Kröll, R. Klieber, and D. Suter, Hole-burning techniques for isolation and study of individual hyperfine transitions in inhomogeneously broadened solids demonstrated in Pr3+:Y_2SiO_5, Phys. Rev. B **70**, 214116 (2004).

[37] B. Lauritzen, S. R. Hastings-Simon, H. De Riedmatten, M. Afzelius, and N. Gisin, State preparation by optical pumping in erbium-doped solids using stimulated emission and spin mixing, Phys. Rev. A **78**, 043402 (2008).

[38] M. Afzelius, I. Usmani, A. Amari, B. Lauritzen, A. Walther, C. Simon, N. Sangouard, J. Minar, H. DeRiedmatten, N. Gisin, and S. Kröll, Demonstration of Atomic Frequency Comb Memory for Light with Spin-Wave Storage, Phys. Rev. Lett. **104**, 040503 (2010).

[39] N. Sinclair, E. Saglamyurek, H. Mallahzadeh, J. A. Slater, M. George, R. Ricken, M. P. Hedges, D. Oblak, C. Simon, W. Sohler, and W. Tittel, Spectral Multiplexing for Scalable Quantum Photonics Using an Atomic Frequency Comb Quantum Memory and Feed-Forward Control, Phys. Rev. Lett. **113**, 053603 (2014).

[40] I. Baumann, R. Brinkmann, M. Dinand, W. Sohler, L. Beckers, C. Buchal, M. Fleuster, H. Holzbrecher, H. Paulus, K. H. Müller, and T. Gog, Erbium incorporation in $LiNbO_3$ by diffusion-doping, Appl. Phys. A **64**, 33 (1996).

[41] F. Marsili, V. B. Verma, J. A. Stern, S. Harrington, A. E. Lita, T. Gerrits, I. Vayshenker, B. Baek, M. D. Shaw, R. P. Mirin, and S. W. Nam, Detecting single infrared photons with 93% system efficiency, Nat. Phot. **7**, 210 (2013).

[42] J. Jin, M. G. Puigibert, L. Giner, J. A. Slater, M. R. Lamont, V. B. Verma, M. D. Shaw, F. Marsili, S. W. Nam, D. Oblak, and W. Tittel, Entanglement swapping with quantum-memory-compatible photons, Phys. Rev. A **92**, 012329 (2015).

[43] A. Kuzmich, W. P. Bowen, A. D. Boozer, A. Boca, C. W. Chou, L. M. Duan, and H. J. Kimble, Generation of nonclassical photon pairs for scalable quantum communication with atomic ensembles, Nature **423**, 731 (2003).